Supplementary Information (SI) for Nanoscale.

Machine Learning-Aided 3D-AFM for Identification of Spatial Heterogeneity in Interfacial Solvation Structures

Supplementary Information

Jiacheng Li[1,2], Zehao Li[1,2], Zhi Xu[1,2], Changlong Ruan[3], Jinhu Yang[3,4], Han Li[1,2,5*], Ming Ma[1,2,5*]

[1]Department of Mechanical Engineering, State Key Laboratory of Tribology in Advanced Equipment (SKLT), Tsinghua University, Beijing 100084, China

[2]Center for Nano and Micro Mechanics, Tsinghua University, Beijing 100084, China

[3]Institute of Engineering Thermophysics, Chinese Academy of Science, Beijing, 100190, China

[4]CAS Aerostar Technology Co., Ltd, Qingdao, 266400, China

[5]Institute of Superlubricity Technology, Research Institute of Tsinghua University in Shenzhen, Shenzhen 518118, China

In this supplementary information, we provide additional details on certain aspects of the study reported in the manuscript. The following issues are discussed:

1. Data Preprocessing
2. Technical Details of the Machine Learning
3. Details of molecular dynamic (MD) simulations
4. Technical Details and Experimental Results Under Different Potentials
5. Validation of Interfacial Heterogeneity via Energy Dissipation
6. Characterization of Interfacial Domain Morphology at Microscale

1. Data Preprocessing

1.1 Spatial Resampling and Feature Dimensionality Reduction

To optimize the performance and robustness of the machine learning framework, the dimensionality of the raw force-distance profiles is reduced from 1500 to 100 features. This is achieved by interpolating the raw data onto a common set of 100 equidistant points across the 3 nm range. This preprocessing step serves three critical functions:

Feature Alignment: Unsupervised algorithms, such as Hierarchical Cluster Analysis (HCA)(1), necessitate that each column in the input matrix represents a consistent physical parameter. By resampling onto a standardized grid, we ensure that the n-th column of the feature matrix corresponds strictly to the physical position $z = n \times 0.03$ nm, providing the necessary foundation for accurate Euclidean distance calculations.

Mitigating the Distance Concentration Effect(2): In extremely high-dimensional spaces (e.g., 1500 dimensions), the contrast between the maximum and minimum Euclidean distances between data points tends to vanish, a phenomenon known as distance concentration. This renders unsupervised algorithms, such as Hierarchical Cluster Analysis (HCA), incapable of discerning meaningful differences between force profiles, as every profile appears equally distant from others. By reducing the dimensionality, we restore the contrast within the feature space, ensuring that distance metrics remain effective for identifying physical patterns of interfacial solvation.

Addressing Data Sparsity and Cluster Stability: As dimensionality increases, the volume of the feature space expands exponentially, causing data points to become increasingly isolated. For a dataset of 8,192 profiles, a 1500-dimensional space is too vast to maintain the "sample density" required for meaningful neighbor relationships. Downsampling to 100 dimensions effectively increases the sample density within the latent space, allowing the clustering algorithm to identify stable and physically relevant clusters while maintaining a sufficient physical resolution of 0.03 nm per point to capture structural details.

1.2 Baseline Correction and Structural Phase Alignment via Cross-correlation

To accurately resolve the spatial distribution of solvation structures, it is imperative to eliminate instrumental artifacts such as thermal drift and phase shifts caused by substrate topography. This processing stage ensures that the resolved oscillating features represent genuine interfacial molecular organization rather than geometric or electronic fluctuations.

Baseline Correction: at large separation distances, the interaction between the AFM tip and the sample should theoretically vanish. However, experimental signals often exhibit vertical baseline offsets due to thermal drift(3). Extraction of Zero-level: For each resampled profile, the far-field non-contact region is identified using the final 10 data points (corresponding to z≈3 nm). Normalization: The mean value of this far-field region is calculated and subtracted from the entire profile, effectively shifting the baseline to zero. This ensures that all analyzed curves possess a consistent reference point in the bulk liquid environment before the onset of solvation forces.

Structural Phase Alignment via Cross-correlation: even on atomically flat surfaces like graphite, nanoscale local roughness or slight sample tilt can lead to phase discrepancies in the z-axis for solvation layers measured at different xy locations. Direct clustering without alignment would lead to "smearing" of the fine oscillatory features. Reference Selection: The algorithm identifies a reference profile (f_{ref}) characterized by the maximum standard deviation (oscillation energy) across the entire 3D dataset. This ensures that alignment is performed against the most distinct structural features. Cross-correlation Algorithm: To determine the optimal vertical shift (τ) for a given curve $g(z)$ relative to the reference $f_{ref}(z)$, a discrete cross-correlation function is employed:

$$R_{fg}(\tau) = \sum_{n} f_{ref}(n) \cdot g(n-\tau)$$

Phase Compensation and Constraints: The optimal lag is identified by finding the maximum value of $R_{fg}(\tau)$. The maximum allowed shift is strictly constrained to ±10 data points (±0.3nm), corresponding approximately to the diameter of a single water molecule(4). The reliability of the structural alignment process is validated through integrated statistical and spatial analyses, as detailed in the Supplementary figures. As illustrated by the distribution of alignment shifts (figure S1), the near-central histogram confirms that the majority of force profiles required only minimal adjustment, indicating that the alignment captured a consistent physical trend across the entire dataset. Complementing this, the 2D alignment shift map (figure S2) reveals characteristic horizontal banding patterns. These spatial features correlate directly with the typical thermal drift encountered along the slow-scanning axis in high-resolution AFM(5), demonstrating that the cross-correlation algorithm successfully compensates for real-time experimental artifacts rather than introducing random noise. By systematically recording these variations in shift_records, we effectively decouple the mechanical solvation signals from the underlying geometric height variations, enabling a purified analysis of interfacial molecular organization independent of topographic interference.

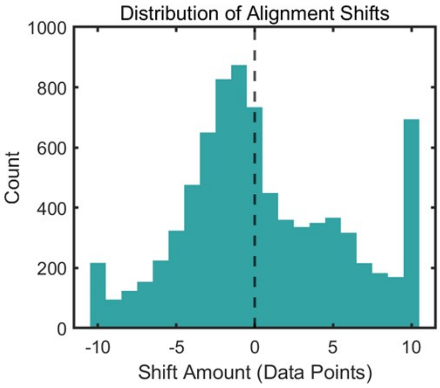

Figure S1. The distribution of alignment shifts map

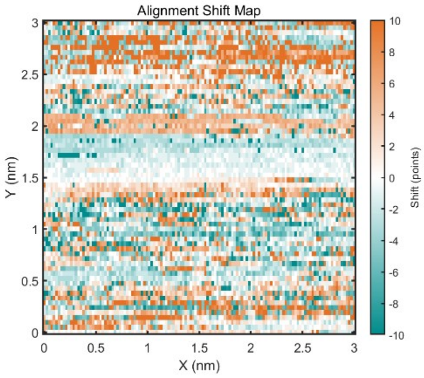

Figure S2. 2D alignment shift map

1.3 Data Cleaning and Outlier Removal

Despite the rigorous preprocessing described above, 3D-AFM datasets often contain a small fraction of non-physical signals resulting from stochastic events such as tip-sample instabilities, micro-bubble interference, or extreme fluctuations of environmental contaminants(6). To prevent these outliers from introducing artifacts into the unsupervised machine learning framework, we implemented an automated cleaning protocol based on the statistical distribution of Euclidean distances.

Specifically, an ensemble mean profile is first established as a global reference to calculate the Euclidean distance for each individual profile across the 3D volume. Following the Pauta criterion (3σ rule)(7), a rejection threshold is strictly defined as the mean distance plus three standard deviations ($T = \mu_D + 3\sigma_D$), ensuring a robust statistical foundation for identifying profiles that deviate significantly from the characteristic solvation behavior.

The efficacy of this outlier detection is validated in Supplementary figure S3, where the scatter plot reveals that out of 8,192 original profiles, only 50 curves (approximately 0.6%) exceeded the 3σ threshold and are consequently excluded (orange markers). These rejected profiles typically represent transient instrumental instabilities or localized contaminants that do not reflect the intrinsic solvation structure. Furthermore, the distance distribution histogram exhibits a well-defined near-normal profile with a narrow spread, underscoring the high fidelity and consistency of the acquired experimental data. This minimal yet precise rejection rate ensures that the finalized dataset for Hierarchical Cluster Analysis (HCA) remains physically grounded while maintaining maximum statistical integrity.

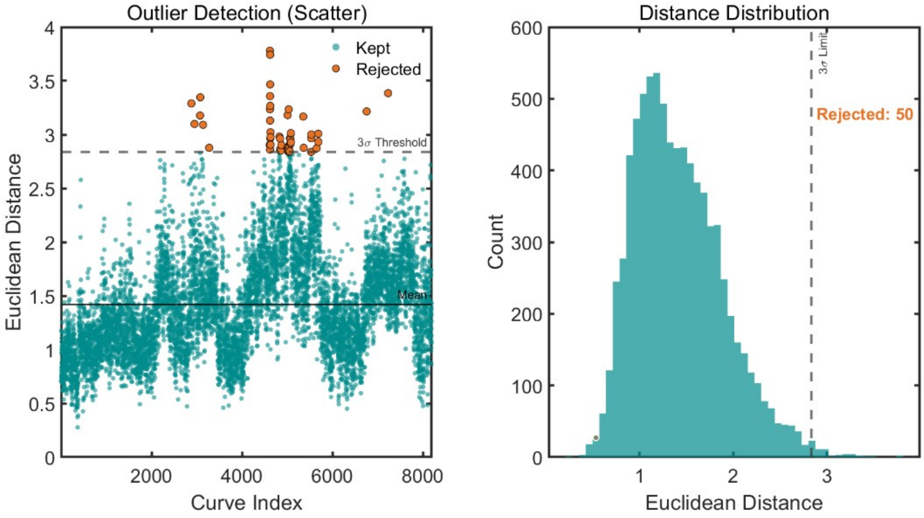

Figure S3. Outlier detection scatter and distance distribution map

2. Technical Details of the Machine Learning

2.1 Hierarchical Cluster Analysis (HCA) Implementation

The unsupervised classification of the interfacial solvation states is conducted using a Hierarchical Cluster Analysis (HCA) framework. This architecture is chosen to decode the complex spatial heterogeneities of the graphite-water interface by organizing the force profiles into a deterministic nested hierarchy based on their intrinsic structural similarities.

A. Similarity Metric: Euclidean Distance

The unsupervised classification is performed on the refined feature matrix $M \in R^{N \times 100}$, where N represents the number of valid force profiles after outlier removal. The similarity between any two force profiles, p_i and p_j, is quantified by the **Euclidean distance**(8):

$$d(p_i,p_j) = \sqrt{\sum_{k=1}^{100} (F_{i,k} - F_{j,k})^2}$$

Where $F_{i,k}$ represents the force value of the k-th point on the i-th curve. This metric is physically significant in the context of 3D-AFM as it ensures that the clustering algorithm is highly sensitive to both the absolute magnitude and the spatial phase of the solvation oscillations.

B. Linkage Criteria: Ward's Minimum Variance Method

Among various hierarchical linkage criteria, Ward's minimum variance method(9) is preferred for this study. The primary objective of Ward's linkage is to minimize the total within-cluster Error Sum of Squares (ESS) at each fusion step. The ESS is mathematically defined as:

$$ESS = \sum_{i=1}^{n} \left(x_i - \bar{x}\right)^2$$

where $x_i$represents the i-th force profile in a cluster and $\bar{x}$ denotes the cluster centroid (mean force profile). At each iteration, the algorithm merges the pair of clusters that results in the minimum increase in ESS, effectively maintaining maximum internal homogeneity.

C. Merging Cost and Physical Rationale

The merging cost (distance increment) between two clusters is as shown in the formula in the main text. The preference for Ward’s method over other partitioning techniques (e.g., K-means) or linkage criteria (e.g., single or complete linkage) is based on several factors(9): a. shape and gradient priority: Ward’s method prioritizes the similarity in the overall shape and gradient of the solvation oscillations rather than just the absolute distance between individual data points. B. deterministic multi-scale analysis: Unlike centroid-based partitioning, HCA provides a deterministic structure that allows for the inspection of the interface's intrinsic multi-scale organization without sensitivity to initial centroid selection. C. cluster morphology: Ward’s method is known to produce clusters of roughly equal size and high spherical density, which is ideal for identifying discrete, stable physical regimes (e.g., water-dominated vs. contaminant-dominated areas) at the solid-liquid interface.

D. Dendrogram Construction and Truncation

This systematic pipeline constructs a tree-like dendrogram reflecting the dataset’s intrinsic topological structure. The vertical axis of the dendrogram represents the Euclidean distance at which clusters are merged. For visual clarity, the hierarchy of the 8,192 individual profiles is truncated to display the top 50 leaf nodes. A large vertical gap between the primary branches indicates a robust and natural separation of the dataset into two distinct solvation regimes, confirming the validity of the K=2 partition.

2.2 Determination of Optimal Clusters (*K*)

Identifying the optimal number of clusters is essential to balance descriptive power and model parsimony. We primarily utilized the Elbow Method(10), complemented by additional cross-validation metrics, to rigorously justify our classification.

The Elbow Method evaluates the Sum of Squared Errors (SSE) as a function of the number of clusters, *k*. The SSE quantifies the total dispersion of data points from their respective cluster centroids and is defined as(10):

$$SSE = \sum_{j=1}^{K} \sum_{x \in C_j} ||x - \mu_j||^2$$

where x is a force profile in cluster C_j, and μ_j is its centroid. While SSE naturally decreases as *k* increases, the rate of reduction markedly drops once the optimal *k* is reached, creating a distinct "inflection point" or "elbow". This point represents the threshold of diminishing returns, where adding more clusters no longer significantly improves the variance explanation of the dataset.

For the results at the water-graphite interface, the SSE-*k* plot is demonstrated in figure S4, where a sharp kink is observed at *k*=2. This indicates that a dual-regime partition is sufficient to capture the fundamental physical heterogeneities of the interface. Increasing the cluster count beyond this value results in a flattened SSE decay, suggesting that higher *k* values primarily model stochastic fluctuations rather than distinct physical states.

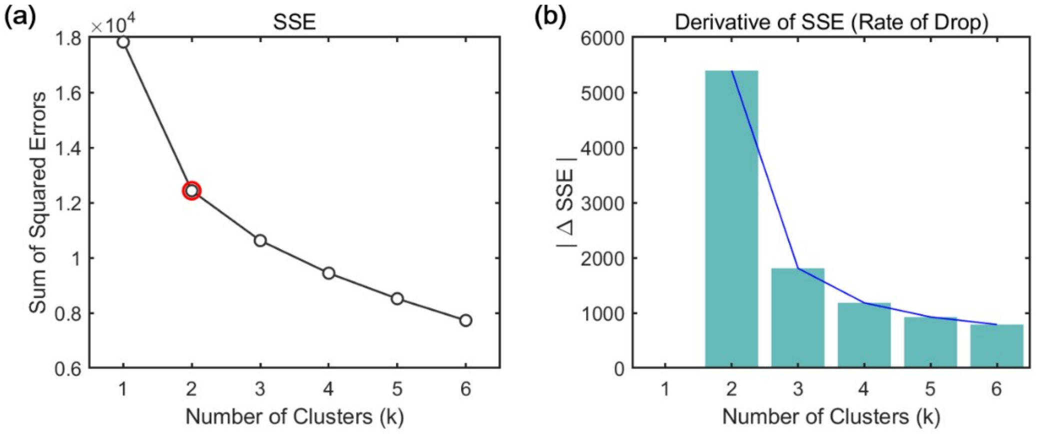

Figure S4. The Elbow Method (SSE) plot at the water-graphite interface. (a)SSE-*k*; (b) △SSE-*k*.

To further ensure the integrity of our clustering, we incorporated Silhouette Analysis(11) as a cross-validation tool. The Silhouette coefficient measures how similar an individual profile is to its own cluster (cohesion) compared to other clusters (separation). Ranging from -1 to 1, a high average silhouette score indicates that the clusters are well-defined and separated. For the water-graphite interface, the result is shown in figure S5. Across the evaluated range of *k*=2 to 6, the mean Silhouette score reaches a distinct global maximum at *k* =2 (approximately 0.3, marked with a red star). This peak indicates that a two-regime partition achieves the optimal balance of cluster cohesion and geometric separation in the feature space. The sharp decline in Silhouette scores for *k*≥3, which then plateau at approximately 0.18, confirms that higher-order partitions lead to over-fragmentation and diminished internal consistency. This cross-validation mirrors the results of the Elbow Method, collectively establishing *k*=2 as the most physically and mathematically sound representation of the interfacial solvation heterogeneities.

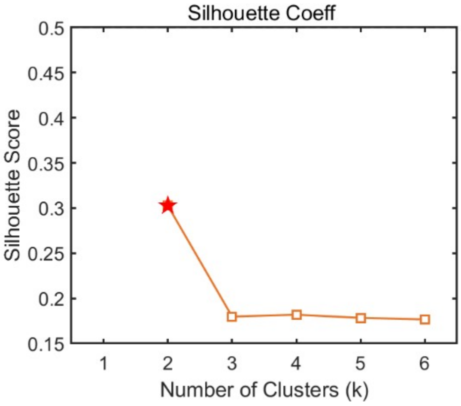

Figure S5. Evaluation of clustering quality via Silhouette Coefficient.

2.3 Diagnostic Manifold Visualization (t-SNE): Theory and Parameterization

To provide an intuitive validation of the HCA results, we employed t-distributed Stochastic Neighbor Embedding (t-SNE)(12), a non-linear dimensionality reduction technique specialized in preserving local pairwise similarities within high-dimensional manifolds.

PCA Pre-compression and Denoising: Prior to t-SNE embedding, the standardized feature matrix is projected onto the first 50 principal components. This step serves a dual purpose: it extracts the primary physical signatures by retaining most of the total variance while effectively filtering out high-frequency stochastic noise inherent in AFM measurements. This pre-compression significantly stabilizes the embedding process and prevents the manifold from being dominated by redundant or noisy dimensions.

Computational Efficiency via Barnes-Hut: Given the large-scale nature of the 3D-AFM dataset (8,192 profiles), we utilized the Barnes-Hut algorithm(13). This optimization reduces the computational complexity from $O(N^2)$ to $O(NlogN)$(13), enabling the efficient processing of thousands of force profiles while maintaining the global topological integrity of the data distribution.

Physical Significance of Perplexity: The Perplexity is set to 30, acting as a smooth measure for the effective number of neighbors considered during manifold construction. This value is carefully chosen to balance the preservation of local structural motifs (e.g., specific solvation peak oscillations) against the broader global relationships between clusters. A perplexity of 30 ensures that the 2D mapping remains continuous and representative of the underlying physical regimes without excessive fragmentation.

KL Divergence and the Crowding Problem: t-SNE employs a Student's t-distribution in the low-dimensional space to mitigate the "crowding problem" typically encountered in traditional MDS or PCA visualizations. By minimizing the Kullback-Leibler (KL) divergence between the high-dimensional and low-dimensional probability distributions, the algorithm ensures that force profiles belonging to the same HCA cluster are tightly clustered, while distinct physical regimes remain clearly separated by wide margins.

Reproducibility: Due to the stochastic nature of the t-SNE optimization process, the random number generator is initialized with a fixed seed (rng(42)). This ensures that the resulting 2D embedding is strictly reproducible and consistent across different computational environments, a critical requirement for rigorous scientific reporting.

3. Details of molecular dynamic (MD) simulations

3.1 Force field MD simulations

To elucidate the molecular-level origins of the interfacial solvation structures, all-atom molecular dynamics (MD) simulations are performed using the LAMMPS package(14). Two model systems are constructed: (i) a pristine graphite–water interface (pure water), and (ii) an interface contaminated with octane (water/octane mixture). This setup allows direct comparison between an ideal, clean interface and one perturbed by a non-polar pollutant.

The graphite substrate is modeled as two layers of rigid graphene sheets with a C–C bond length of 0.142 nm, where interlayer interactions are governed by the Lennard-Jones (L-J) potential. Water molecules are described using the SPC/E model(15), while octane molecules and their associated interaction parameters follow the CHARMM36 all-atom force field(16). The simulation box dimensions are approximately 3×3×10 nm^3, featuring a liquid reservoir exceeding 5 nm in the z-direction to ensure bulk properties. Additionally, a 5 nm vacuum layer is implemented along the z-axis to mitigate artifacts arising from long-range Coulombic interactions under periodic boundary conditions.

The simulations are performed in the NVT ensemble with the temperature maintained at 298 K. All molecular dynamics runs are carried out using the LAMMPS package with a time step of 1 fs. A Lennard-Jones (LJ) potential is employed, modified by a switching (or shifting) function to smoothly bring the energy or force to zero between an inner cutoff of 1.0 nm and an outer cutoff of 1.2 nm. The interaction describing water–carbon interactions is taken from (16), and the contact angle of water on the graphene surface is 86°. Long-range electrostatic interactions are handled via the Particle-Particle Particle-Mesh (PPPM)(17) algorithm with a cutoff radius of 1.2 nm. For the water/octane mixture, a total simulation time of 20 ns is employed, with data sampling conducted over the final 10 ns following a 10 ns equilibration period; the pure water system reaches equilibrium more rapidly and is simulated for a total of 10 ns.

3.2 Analysis for liquid structure

The mass density profiles $\rho(z)$ are computed by systematically identifying liquid atoms and assigning their elemental masses (C: 12.011, O: 15.999, H: 1.008 amu) while excluding the rigid graphite substrate via a logical indexing protocol. To ensure statistical convergence, the analysis utilized the stabilized segments of the production trajectories—specifically the final 1000 frames for system—to account for the different relaxation timescales of the interfacial layers. The liquid domain is partitioned into 100 discrete spatial bins along the z-axis, where the cumulative mass in each bin is calculated using the "accumarray" function and normalized by the bin volume (Area $\times \Delta z$) and total frame count. The resulting raw density values are converted to macroscopic units (g/cm^3)and further refined with a 4-point moving average to resolve reliable density gradients independent of stochastic sampling noise.

In the present study, the Solvent-Tip Approximation (STA) model is utilized to transform liquid density profiles into solvation forces(18).

$$F(z) = \left(\frac{k_B T}{\rho(z)}\right) \cdot \left(\frac{d\rho}{dz}\right)$$

Where $F(z)$ is the force, k_B is the Boltzmann constant, T is the absolute temperature, $\rho(z)$ is the local mass density of the solvent at a specific distance z from the substrate, $d\rho/dz$ is The spatial density gradient of the solvent along the z-axis. The STA model serves as a pivotal simplified framework linking the density distribution of solvation structures to interfacial solvation forces, with the primary advantage of enabling the quantitative conversion of microscopic density data into macroscopic force signals without the need for computationally intensive multi-body interaction simulations. Grounded in the principles of statistical mechanics, this model approximates the atomic force microscopy (AFM) tip as a single solvent molecule. By establishing a quantitative correlation between the local solvent density and the resulting interaction forces, the interfacial solvation force can be derived directly from the structural density distribution of the solvation layers. The fundamental logic dictates that the solvation force originates from the density fluctuations of solvent molecules within the interfacial region. The STA model simplifies this complex phenomenon through the Boltzmann statistical relationship, thereby facilitating the efficient calculation of interfacial solvation interaction forces based solely on the density distribution data.

3.3 Validation of Interfacial Heterogeneity via Multi-Species MD Simulations

To further substantiate the identification of the two experimentally resolved interfacial regimes, we performed additional MD simulations involving a broader variety of hydrocarbon contaminants. Specifically, we extended our computational model to include figure S6(a) water with 40% octane system and figure S6(b) water with 20% hexane system on a graphite substrate.

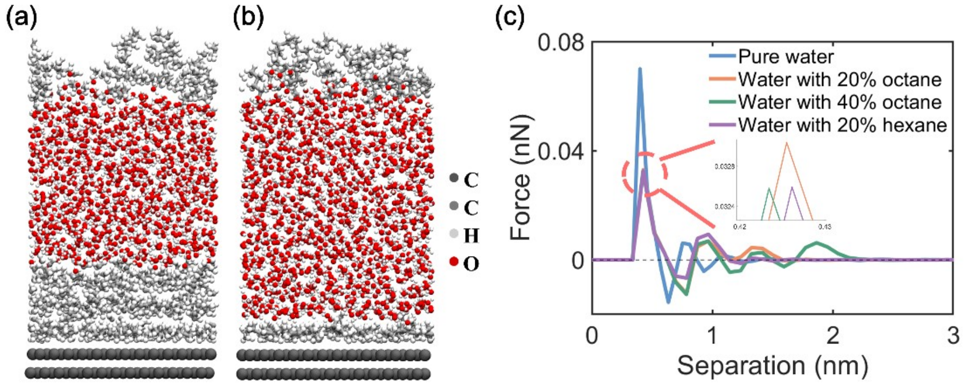

Figure S6. (a) Molecular dynamics snapshots of the water with 40% octane system on a graphite substrate. (b) Molecular dynamics snapshots of the water with 20% hexane system on a graphite substrate. (c) Calculated solvation force curves under different systems.

The force-distance profiles derived from these simulations were processed using the STA models (figure S6(c)). Our results demonstrate that regardless of the hydrocarbon species (octane vs. hexane) or concentration (20% vs. 40%), the simulated force-distance curves exhibit a consistent trend: a significant reduction of the first solvation peak, followed by a non-oscillatory decay.

As shown in Figure S6(c), the pristine water–graphite interface exhibits a sharp and oscillatory hydration layering. In contrast, all hydrocarbon-covered interfaces display a significant reduction in their first peak amplitude. Specifically, the first force peak displays a 57% reduction relative to the pristine water system. This simulated 57% reduction is independent of both the hydrocarbon species and concentration, which is in excellent agreement with the 54% reduction observed experimentally between the two clusters.

The results from these extended MD simulations show excellent agreement with our experimental 3D-AFM clustering analysis. When combined with the established literature trends on hydrocarbon evolution, the physical identity of the two resolved regions becomes clear. Cluster 1 represents the intrinsic structured water interface, while Cluster 2 captures the hydrocarbon-dominated regime. This convergence of simulation, experiment, and prior literature confirms that the two clusters reflect a fundamental interfacial transition rather than minor variations within different hydrocarbon sub-phases.

3.4 Potential-Dependent MD Simulations and Experimental Validation

To elucidate the experimental observations regarding the potential dependence of the interfacial solvation structures, we performed additional MD simulations incorporating a constant potential method. In our initial computational framework, the system was simulated under zero charge density. Here, we extended the model to capture the effect of graphite electrification on the water-alkane-graphite interface at an applied potential of 800 mV.

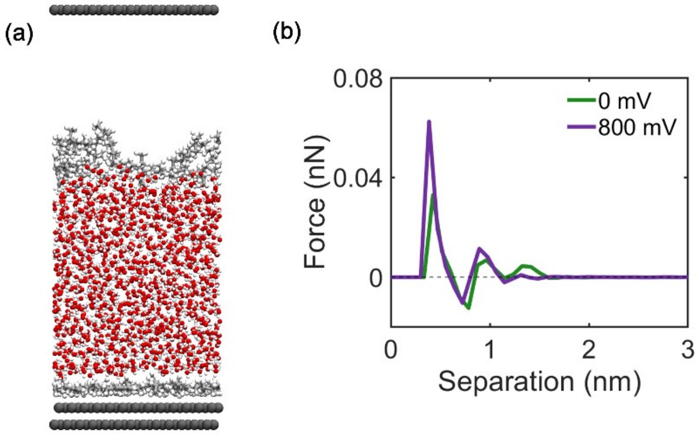

Figure S7. Constant-potential molecular dynamics (MD) simulation setup and potential-dependent mechanical response. (a) Snapshot of the atomistic electrochemical cell model. (b) solvation force-distance profiles simulated under substrate potentials of 0 mV (green) and 800 mV (purple).

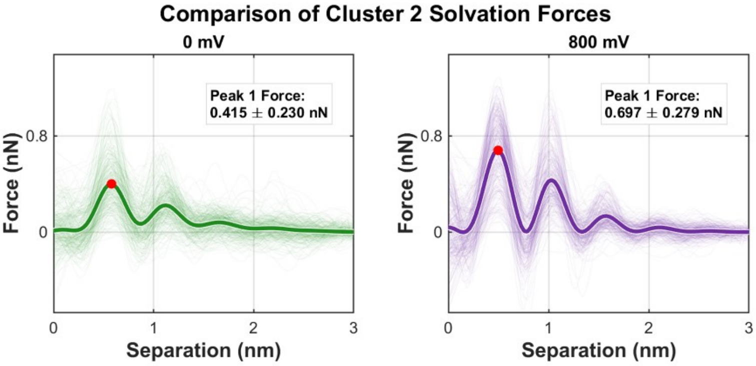

Figure S8. Experimental potential-dependent solvation force of Cluster 2.

The constant potential environment was implemented using the ELECTRODE package in LAMMPS. To construct the electrochemical cell setup (schematically illustrated in figure S7(a)): An additional, atomistic graphene layer was introduced at the top of the vacuum region to serve as the counter-electrode. To ensure that this auxiliary layer serves exclusively to balance the electrostatic charges without introducing non-physical physical constraints, the Lennard-Jones interaction parameters between this top electrode and all other system components (including water, alkanes, and the bottom graphite substrate) were strictly set to zero. During the production runs, the electrical potential of the bottom graphite substrate was fixed at a constant value of 800 mV, while the top counter-electrode was grounded at 0 mV. All other interatomic potentials, ensembles, and thermodynamic control parameters remained identical to the baseline models described in Section 3.1.

The force-distance profiles extracted from the potential-dependent MD simulations were transformed using the STA model to allow a direct comparison with the experimental 3D-AFM statistical curve subsets for Cluster 2.

As shown in Figure S8, the experimental 3D-AFM force spectroscopy profiles exhibit a pronounced response to the applied substrate bias. At 0 mV, the statistical mean force of the primary solvation peak for Cluster 2 is 0.415±0.230 nN. Upon polarizing the substrate to 800 mV, the primary peak force noticeably increases to 0.697±0.279 nN, which corresponds to a relative mechanical enhancement of 68.0%. This potential-induced strengthening effect is reproduced by our constant-potential MD simulations (Figure S7(b)). Under zero-bias conditions, the simulated force profile yields a first peak value of 0.033 nN. When the constant potential of 800 mV is applied, the first peak force rises to 0.062 nN, representing a relative enhancement of approximately 87.9%. While the absolute magnitudes of the forces differ between the experimental measurements and the atomistic simulations—a common disparity arising from the spatial constraints of the simulation box, the idealized spring constants, and the coarse-grained nature of classical force fields—the relative scaling trends and enhancement factors are highly comparable (68.0% in experiments vs. 87.9% in simulations).

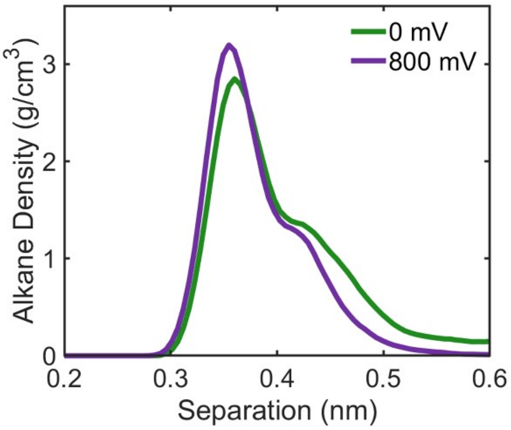

Figure S9. Simulated mass density profiles of alkanes. Comparison of the alkane density distributions near the interface under 0 mV and 800 mV bias potentials.

To further investigate the physical mechanism underlying this potential-induced behavior, we extracted the mass density profiles of the alkanes from MD simulations, as shown in Figure S9. At 800 mV, the first density peak of the alkane layer is located at 0.355 nm with a peak density of 3.195 g/cm^3. In contrast, at 0 mV, the first density peak shifts slightly outward to 0.360 nm with a peak density of 2.849 g/cm^3. Combined with the enhanced solvation forces observed at the higher bias, these simulation results demonstrate that the applied electric field drives a more compact and densely packed adsorption of the alkanes on the substrate. This computational finding is in agreement with our experimental observations, where the contaminant coverage increases under high bias potentials.

This qualitative and semi-quantitative agreement indicates that the applied electrical potential induces a physical mechanism at the interface: the electrification of the graphite surface alters the local electrostatic field, driving a structural reorganization of the interfacial water layers and a redistribution of the localized hydrocarbon contaminants. Consequently, these new simulations provide definitive theoretical backing for our experimental assignments, confirming that the potential sensitivity of Cluster 2 is an intrinsic property governed by the electrified graphite-fluid interface physics.

4. Technical Details and Experimental Results Under Different Potentials

4.1 Localized Two-Electrode Configuration and Hardware Mechanisms

To evaluate the response of the interfacial heterogeneity to external electrical stimuli, 3D-AFM force mapping was conducted across a wide potential window. In this study, a two-electrode system was implemented. This specialized configuration is schematically illustrated in figure S10.

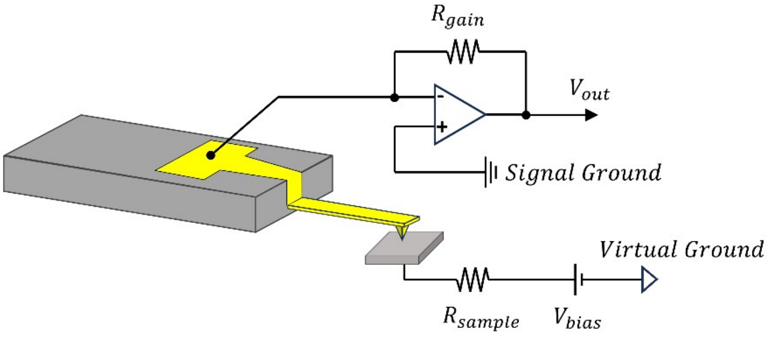

Figure S10. Schematic diagram of the localized two-electrode circuit setup

The conductive gold-coated AFM probe functions concurrently as both the Counter Electrode (CE) and the Reference Electrode (RE). Through the active transimpedance circuitry, the probe tip is maintained strictly at a stable ground (0 V). Meanwhile, the underlying graphite substrate serves as the Working Electrode (WE), where the external DC bias voltage is applied directly via the liquid cell stage. Consequently, this precise configuration guarantees that the full potential difference across the sub-nanometer tip-sample gap is directly dictated by the nominal bias voltage.

This two-electrode setup is strategically adopted due to the highly constrained spatial geometry of the AFM liquid cell. In existing interfacial studies, this two-electrode setup is widely accepted and adopted(19-22). Specifically, Acharya et al. adopted a two-electrode setup to investigate the electric-field-mediated modulation of interfacial friction and slip characteristics of TiO_2 and Al_2O_3 nanoparticle aqueous suspensions on platinum surfaces(19). Similarly, Zhang et al. implemented a similar two-electrode configuration to resolve the interfacial water molecular structures on graphite surfaces regulated by an applied potential(20).

We emphasize that the objective of this potential-dependent investigation is to study the non-Faradaic, electrostatic modulation of neutral interfacial contaminants under an external electric field, rather than driving Faradaic electrochemical reactions. Unlike standard electrochemical studies targeting redox reaction kinetics, our study relies on the field-driven displacement and relative shifts in spatial occupancy to identify phase transitions. Because the steady-state leakage current in this non-Faradaic regime is negligible, the ohmic voltage drop across the micro-volume cell is completely minimized, and the nominal applied voltage efficiently drops across the immediate interface. Therefore, the local two-electrode configuration is fully sufficient and robust for capturing the fundamental physical response of the interface.

4.2 Experimental Results Under Different Potentials

To verify the generalizability and robustness of the proposed unsupervised machine learning method, we extended the 3D-AFM measurements and the identical HCA processing workflow to the graphite–water interface under a broad electrochemical window ranging from −800 mV to +800 mV. The substrate potential was adjusted in a stepwise manner following a specific alternating sequence: 800, -800, -400, 400, 200, -200, -100, and 100 mV. This sequence was designed to monitor the reorganization of the solvation structure as the surface charge density was gradually reduced, while also allowing us to assess the stability of the adsorbed species under fluctuating field polarities. Supplementary figures S10 and S11 present the raw 3D phase data and the derived 3D force map, respectively. Both sets of data consistently reveal interfacial stratification under varying applied voltages.

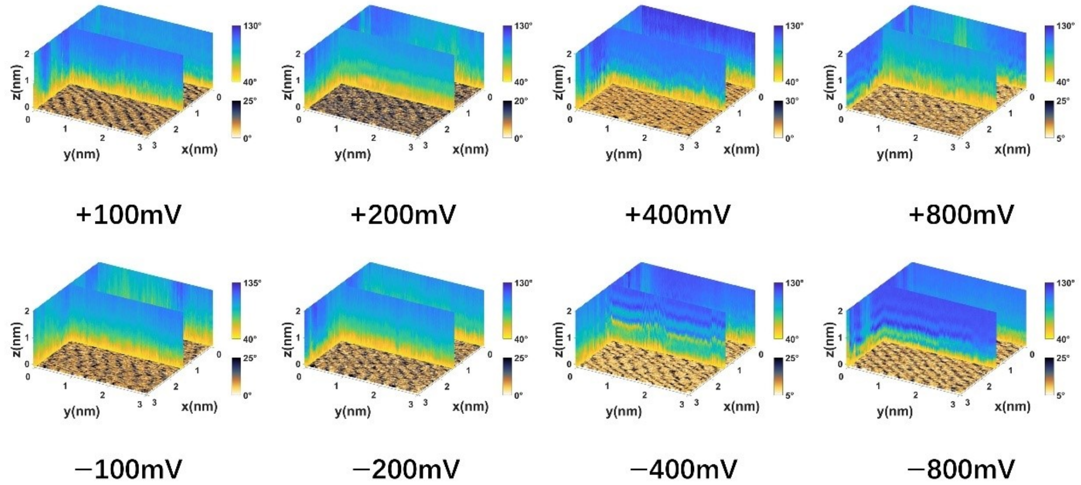

Figure S11. 3D phase image of layered hydration structures (cyan stripes) at the graphite-water interface under different voltages.

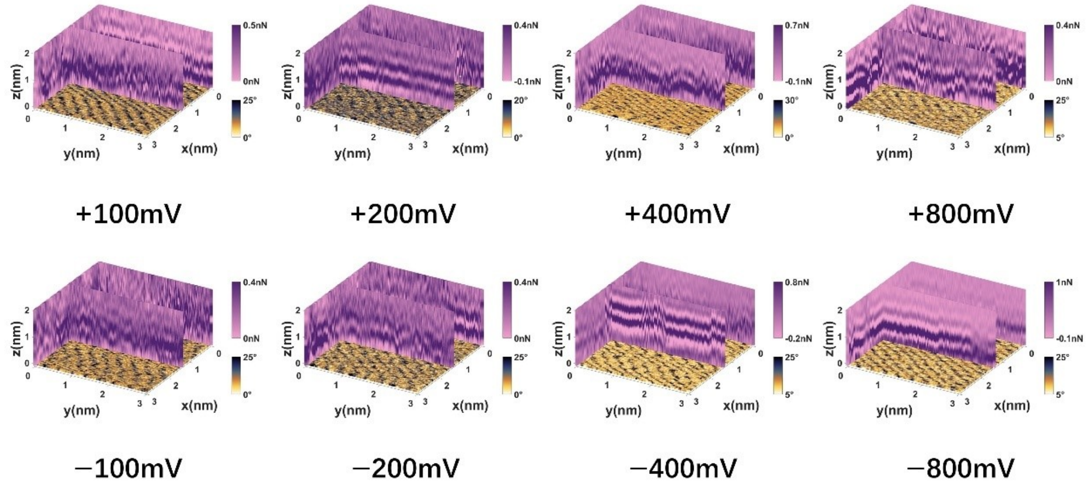

Figure S12. 3D force image of layered hydration structures (cyan stripes) at the graphite-water interface under different voltages.

The resulting Hierarchical Cluster Analysis (HCA) dendrograms (figure S13) and t-SNE visualization maps (figure S14) provide direct structural evidence for the evolution of interfacial heterogeneities. In the HCA dendrograms shown in figure S13, it is observed that the contaminant-dominated regime (orange cluster) exhibits significantly more complex branching structures and increased hierarchical depth at high potential magnitudes. This structural elaboration within the dendrogram is highly consistent with the increased contaminant population observed at high voltages in the main text. Such a trend serves as a robust structural validation of the premise that the high surface charge density induced by elevated potentials enhances the electrostatic attraction toward polar or polarizable pollutants in the environment, thereby promoting their stable adsorption and accumulation at the interface. Furthermore, the branching characteristics in the HCA results manifest a distinct polarity-dependent asymmetry at equivalent voltage magnitudes; specifically, the contaminant clusters under positive potentials exhibit more extensive branching than those under negative potentials. This observation is in excellent agreement with the experimental finding of higher contaminant coverage at positive biases, further corroborating the existence of a preferential interaction between the hydrocarbon species and the positively charged graphite surface. Such an effect is likely driven by the specific polarizability or localized partial charges of the adsorbed molecules. Concurrently, the t-SNE maps in figure S14 demonstrate that the water-dominated and contaminant-dominated regimes maintain a robust and well-defined topological separation in the manifold space across the entire range of external field stimuli. This persistent separation not only underscores the reliability of our automated classification strategy in dynamic signal environments but also confirms that the non-uniform distribution of hydrocarbon contaminants is a universal feature of the graphite–water interface that intensifies with increasing substrate potential .

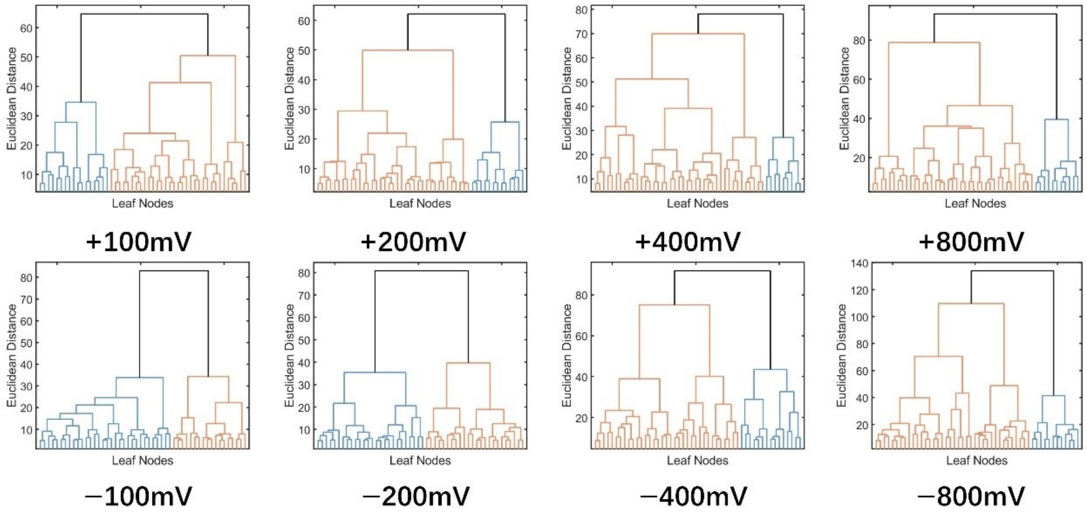

Figure S13. HCA dendrograms at the graphite-water interface under different voltages.

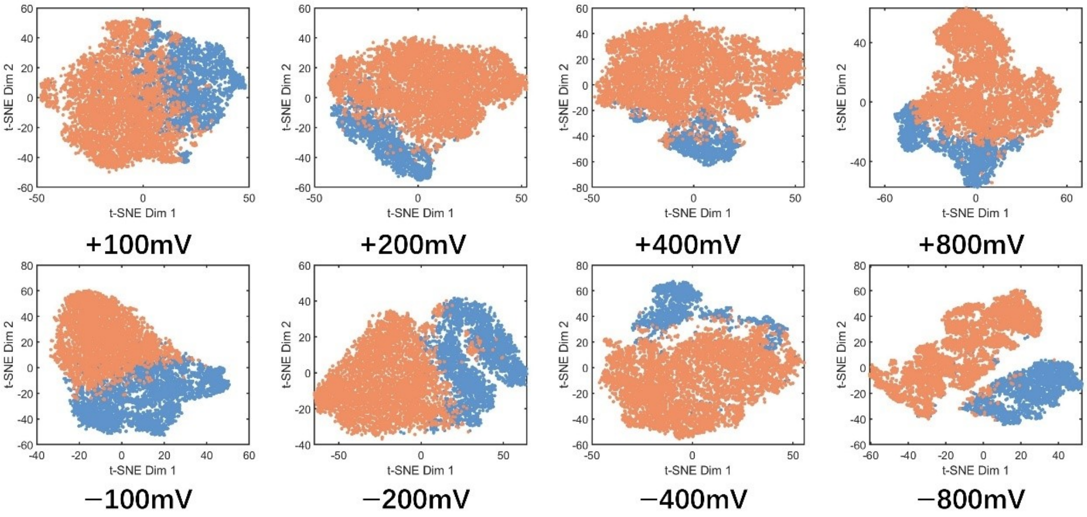

Figure S14. t-SNE visualization map at the graphite-water interface under different voltages.

5. Validation of Interfacial Heterogeneity via Energy Dissipation

To validate the interfacial phase separation identified by force-distance spectroscopy, we performed an auxiliary clustering analysis based on energy dissipation profiles.

Energy dissipation is a thermodynamic descriptor sensitive to the non-conservative processes (e.g., viscous damping and molecular rearrangements) occurring at the solid-liquid interface, which provides a complementary perspective to the conservative force interactions.

5.1 Clustering Methodology and Optimal Classification

The energy dissipation profiles were extracted from the raw amplitude and phase signals using the established theoretical framework(23). Upon obtaining the energy dissipation dataset, we subjected it to the HCA model for further examination. To determine the optimal number of clusters objectively, we employed two standard machine learning validation metrics:

The Elbow Method: By plotting the SSE as a function of *K* (figure S15(a)), we identified the inflection point (the 'elbow') at *K*=2, which signifies the onset of diminishing returns in capturing the dataset's variance. This is further corroborated by the derivative analysis of SSE (figure S15(b)), showing a sharp decline in the rate of change at *K*=2.

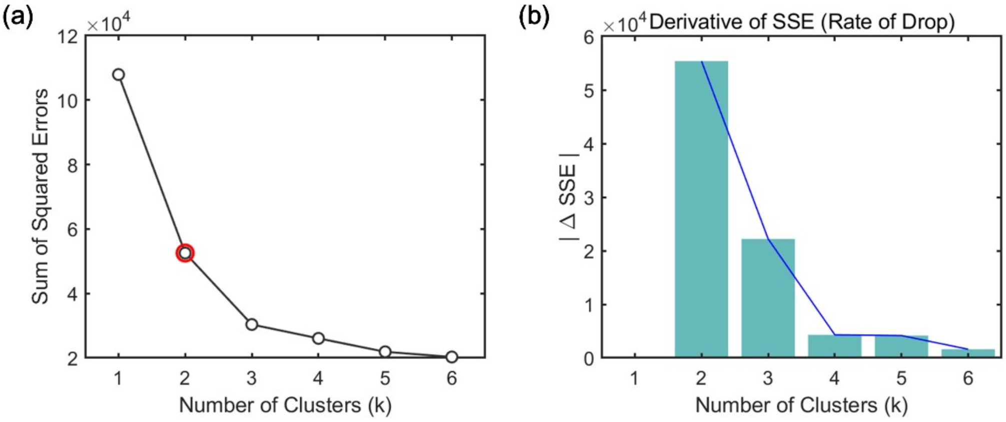

Figure S15. The Elbow Method plot for energy dissipation. (a)SSE-k; (b) △ SSE-*k*.

Silhouette Coefficient Analysis: This metric assesses the cohesion and separation of the clusters (figure S16). The silhouette score reaches its global maximum at *K*=2, confirming that the binary classification provides the most robust and statistically distinct representation of the interfacial state.

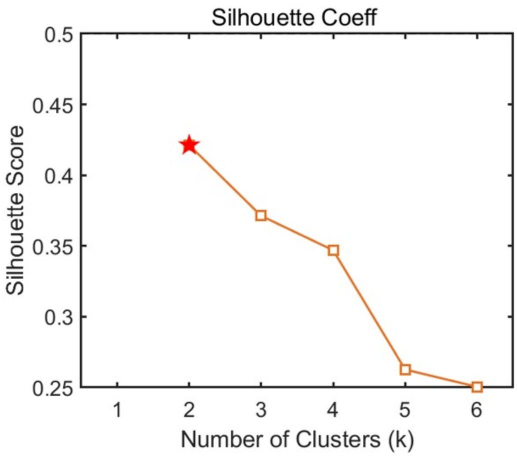

Figure S16. Evaluation of clustering quality via Silhouette Coefficient for energy dissipation.

5.2 Cluster analysis results for energy dissipation

Based on the Ward linkage hierarchical clustering tree (figure S17(a)) and the t-SNE feature space visualization (figure S17(b)), all data points are clearly partitioned into two distinct physical regimes.

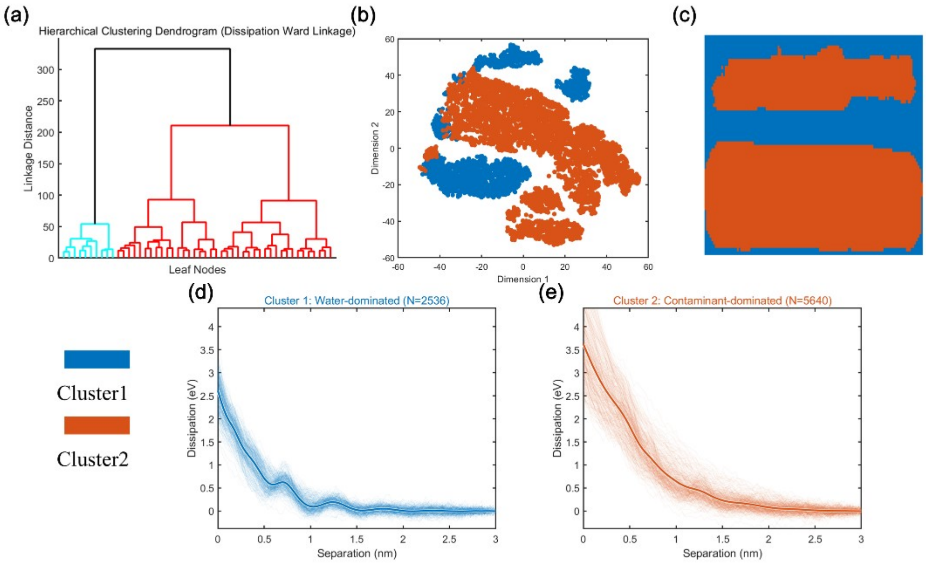

Figure S17. Unsupervised classification and statistical characterization for energy dissipation. (a) Dendrogram of HCA. (b) t-SNE visualization. (c) Spatial clustering map. (d, e) Individual and average energy dissipation profiles for (d) Cluster 1 and (e) Cluster 2.

The resulting 2D spatial distribution map (figure S17(c)) exhibits a high topological correlation with the force-spectroscopy map presented in the main text (Figure 3c). The two identified regimes show distinct mechanical fingerprints (figure S17(d, e)):

Cluster1 (Water-dominated): Characterized by lower overall energy loss and pronounced periodic oscillatory features. These periodic dissipation peaks correspond to the discrete work required to displace the highly ordered, layered water molecules at the interface.

Cluster2 (Contaminant-dominated): Displaying significantly higher energy dissipation without oscillatory motifs. This smooth, high-magnitude damping is a thermodynamic manifestation of the viscoelastic drag and conformational friction induced by the disordered, trapped hydrocarbon layers.

The alignment of the spatial occupancy (approx. 31.0% vs. 69.0%) and the morphological consistency between force and dissipation domains provide unambiguous evidence that the observed interfacial heterogeneity reflects a fundamental physical phase transition rather than experimental artifacts or noise.

6. Characterization of Interfacial Domain Morphology at Microscale

To assess the spatial landscape and statistical robustness of the resolved interfacial heterogeneities, we extended the HCA-based spatial mapping from the nanoscale to a 1×1 um^2 field of view. The resulting large-scale spatial distribution map, generated by projecting the HCA clustering results onto the wider 2D grid, is presented in Figure S18(e).

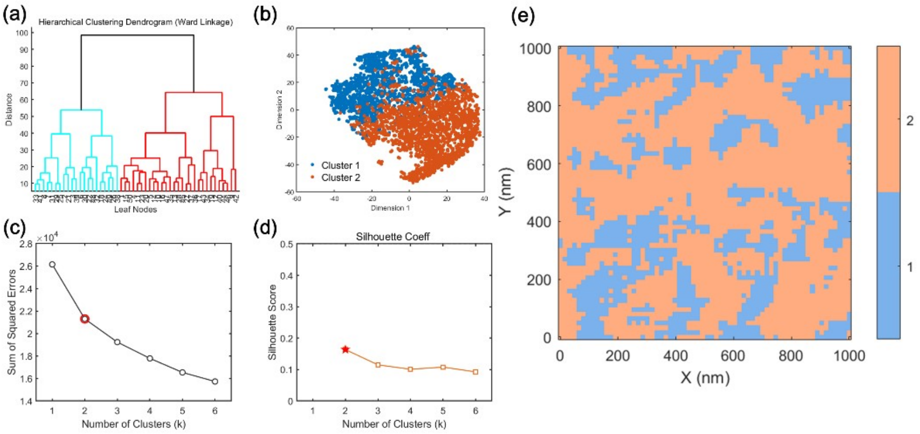

Figure S18. Unsupervised machine learning classification and large-scale spatial mapping at a scale of 1×1 um^2. (a) HCA dendrograms. (b) t-SNE visualization map. (c) SSE as a function of cluster number. (d) Evaluation of clustering quality using the silhouette coefficient. (e) Reconstructed spatial distribution map of the two clusters across the 1×1 um^2 area.

As shown in Figure S18(e), the microscale spatial distribution resolves a complex, patchy, island-like phase separation morphology. The contaminated domains (Cluster 2, orange) form an interconnected, intricate percolation network across the graphite substrate.

The persistence of these complex, microscale domain architectures confirms that the resolved interfacial heterogeneity is independent of the scanning probe trajectory and parameters. If these structures were measurement artifacts such as tip-induced dragging or feedback instability, their morphology would be strictly dictated by the scanning trajectory, appearing as uniform, non-interrupted streaks across the entire image and highly sensitive to scan speed or feedback gain.

The absence of such scan-direction-dependent streaks across the 1×1 um^2 area, combined with the structural stability of the complex domain boundaries, provides robust evidence that these domains represent genuine, Thermodynamic-equilibrium phase separation on the graphite lattice. The "linear-like" features occasionally observed in smaller-scale scans are thus reinterpreted as local subsets or tortuous segments within the larger, complex interfacial network. We conclude that the resolved distinct phase regimes are intrinsic physical features and not artifacts derived from the measurement process.

References

1. Lance GN, Williams WT. A GENERAL THEORY OF CLASSIFICATORY SORTING STRATEGIES .1. HIERARCHICAL SYSTEMS. Computer Journal. 1967;9(4):373-&.

2. Aggarwal CC, Hinneburg A, Keim DA. On the surprising behavior of distance metrics in high dimensional space. In: VanDenBussche J, Vianu V, editors. Database

Theory - Icdt 2001, Proceedings. Lecture Notes in Computer Science. 19732001. p. 420-34.

3. Fukuma T, Garcia R. Atomic- and Molecular-Resolution Mapping of Solid-Liquid Interfaces by 3D Atomic Force Microscopy. Acs Nano. 2018;12(12):11785-97.
4. Israelachvili JN. Intermolecular and Surface Forces Preface to the Third Edition2011. XVII-+ p.
5. Sevim S, Tolunay S, Torun H. Micromachined sample stages to reduce thermal drift in atomic force microscopy. Microsystem Technologies-Micro-and Nanosystems-Information Storage and Processing Systems. 2015;21(7):1559-66.
6. Arvelo DM, Uhlig MR, Comer J, García R. Interfacial layering of hydrocarbons on pristine graphite surfaces immersed in water. Nanoscale. 2022;14(38):14178-84.
7. Levitt BP. AN INTRODUCTION TO ERROR ANALYSIS - THE STUDY OF UNCERTAINTIES IN PHYSICAL MEASUREMENTS - TAYLOR,JR. Journal of the Chemical Society-Faraday Transactions I. 1983;79:2269-.
8. Murtagh F, Farid MM. Pattern classification, 2nd edition. Journal of Classification. 2001;18(2):273-5.
9. Ward JH. HIERARCHICAL GROUPING TO OPTIMIZE AN OBJECTIVE FUNCTION. Journal of the American Statistical Association. 1963;58(301):236-&.
10. Thorndike RL. WHO BELONGS IN THE FAMILY. Psychometrika. 1953;18(4):267-76.
11. Rousseeuw PJ. SILHOUETTES - A GRAPHICAL AID TO THE INTERPRETATION AND VALIDATION OF CLUSTER-ANALYSIS. Journal of Computational and Applied Mathematics. 1987;20:53-65.
12. van der Maaten L, Hinton G. Visualizing Data using t-SNE. Journal of Machine Learning Research. 2008;9:2579-605.
13. Barnes J, Hut P. A HIERARCHICAL O(N-LOG-N) FORCE-CALCULATION ALGORITHM. Nature. 1986;324(6096):446-9.
14. Plimpton S. FAST PARALLEL ALGORITHMS FOR SHORT-RANGE MOLECULAR-DYNAMICS. Journal of Computational Physics. 1995;117(1):1-19.
15. Berendsen HJC, Grigera JR, Straatsma TP. THE MISSING TERM IN EFFECTIVE PAIR POTENTIALS. Journal of Physical Chemistry. 1987;91(24):6269-71.
16. Vanommeslaeghe K, Hatcher E, Acharya C, Kundu S, Zhong S, Shim J, et al. CHARMM General Force Field: A Force Field for Drug-Like Molecules Compatible with the CHARMM All-Atom Additive Biological Force Fields. Journal of Computational Chemistry. 2010;31(4):671-90.
17. Hockney RW, Eastwood JW. Computer simulation using particles1988. xxi+540 p.
18. Miyazawa K, Kobayashi N, Watkins M, Shluger AL, Amano K-i, Fukuma T. A relationship between three-dimensional surface hydration structures and force distribution measured by atomic force microscopy. Nanoscale. 2016;8(13):7334-42.
19. Acharya B, Seed CM, Brenner DW, Smirnov AI, Krim J. Tuning friction and slip at solid-nanoparticle suspension interfaces by electric fields. Scientific Reports. 2019;9.
20. Lalith Krishna Samanth Bonagiri DMA, Fujia Zhao, Jaehyeon Kim, Qian Ai, Shan

Zhou, Kaustubh S. Panse, Ricardo Garcia & Yingjie Zhang. Probing the molecular structure at graphite–water interfaces by correlating 3D-AFM and SHINERS. Nature Communications. 2026.

21. Huang K, Anne A, Bahri MA, Demaille C. Probing Individual Redox PEGylated Gold Nanoparticles by Electrochemical-Atomic Force Microscopy. Acs Nano. 2013;7(5):4151-63.

22. Derylo MA, Morton KC, Baker LA. Parylene Insulated Probes for Scanning Electrochemical-Atomic Force Microscopy. Langmuir. 2011;27(22):13925-30.

23. Hölscher H. Quantitative measurement of tip-sample interactions in amplitude modulation atomic force microscopy. Applied Physics Letters. 2006;89(12).